Nanostructuring Borosilicate Glass With Near-Field Enhanced Energy Using a Femtosecond Laser Pulse

Alex Heltzel

Arvind Battula

J. R. Howell

Shaochen Chen

Department of Mechanical Engineering,
The University of Texas at Austin,
Austin, TX 78712

A model based on the evolution of electron density derived from the Fokker-Planck equation has been built to describe ablation of dielectrics during femtosecond laser pulses. The model is verified against an experimental investigation of borosilicate glass with a 200 fs laser pulse centered at 780 nm wavelength in a range of laser energies. The ablation mechanisms in dielectrics include multi-photon ionization (MPI) and avalanche ionization. MPI dominates the ionization process during the first stages of the laser pulse, contributing seed electrons which supply avalanche ionization. The avalanche process initiates and becomes responsible for the majority of free-electron generation. The overall material removal is shown to be highly dependent upon the optical response of the dielectric as plasma is formed. The ablation model is employed to predict the response of borosilicate glass to an enhanced electromagnetic field due to the presence of microspheres on the substrate surface. It is shown that the diffraction limit can be broken, creating nanoscale surface modification. An experimental study accompanies the model, with AFM and SEM characterizations that are consistent with the predicted surface modifications. [DOI: 10.1115/1.2360595]

Introduction

In the field of optoelectronics and micro-electronics fused quartz and related silicate glasses are very important materials due to their high transmission properties in the UV to IR range, excellent thermal properties, good electrical insulation and high chemical stability [1]. Also, borosilicate glass has an excellent anodic bonding property and surface integrity which makes it the usual substrate for micro-electro mechanical systems (MEMS). Therefore, in order to build a communication interface, micro/nano-holes free of micro-cracks, with good edge and surface quality as well as high aspect ratios need to be formed on the glass substrate. Using traditional micro-machining process for a micro-hole with a diameter below 200 μm is difficult because of the extreme hardness, brittleness, corrosion resistance, and melting temperature of glass. Also the conventional thermal and/or chemical machining methods create an excessive heat-affected zone. Mechanical machining methods also have limitations in productivity and accuracy [2]. Hence, to solve this problem various machining methods have been proposed like the combination of micro electrical-discharge machining and micro ultrasonic vibration machining [3], micro-abrasive jet machining (AJM) [2], laser-induced plasma-assisted ablation (LIPAA) [4], direct laser write laser process using short pulses [5], combination of nanoindenter and hydrofluoric acid wet etching [6], and hologram encoding system with femtosecond laser pulses [7], etc. Due to the various working mechanisms of these methods, the results produced are distinct. However, high-quality holes in nanoscale were not obtained using these techniques.

Laser induced ablation has several advantages over the conventional mechanical and/or chemical machining; it is a single-step process with very high flexibility, noncontact process, direct patterning without the photoresist process, good material removal rate and does not require any etchants. Femtosecond regime offers advantages over the nanosecond regime, by depositing energy into a material in a very short time period, before any thermal diffusion can occur. In this paper we demonstrate a technique wherein, the optical near-field effect is utilized to overcome the diffraction limit to nano-pattern hard-to-machine borosilicate glass using a femtosecond laser. In the first part of the paper we discuss the theoretical background for the study with numerical results. The following part will describe the experimental study where a good agreement between the theoretical and experimental results can be seen.

Theoretical Development

The essentially nonthermal process of femtosecond laser ablation makes it very attractive as a machining tool due to the clean features and negligible heat-affected zone. As a nonthermal process, standard heat transfer models must be discarded in favor of ideas that describe the complex photon energy absorption as well as the mechanisms that transport the energy between the electronic system and lattice system. Several studies have provided empirical data that make a theoretical investigation of ultrafast ablation of dielectrics possible [8–13].

Due to the wide energy gap between the valence and conduction bands of dielectrics, the conduction band is occupied by low electron densities within a large range of electron temperatures. Energy will not be transported by phonons through the dielectric material during a sub-picosecond laser pulse because the free electron thermal relaxation times are generally larger than the pulse duration, leaving lattice temperatures essentially unchanged. For these reasons, the popular two-temperature model [14,15] used for femtosecond laser heating of metals is invalid for dielectric materials or any possessing a sufficiently wide bandgap. To model laser heating in fused silica and borosilicate glass, a rela-

tion derived by Stuart et al. [9] is used, describing the evolution of free electron density in a dielectric medium exposed to intense laser radiation

$$\frac{dn_e(r,z,t)}{dt} = a_i I(r,z,t) n_e(r,z,t) + \delta_N (I(r,z,t))^N \quad (1)$$

where I is the spatial and temporally dependent intensity of the laser pulse, n_e is the electron density, a_i is the avalanche ionization coefficient, and δ_N is the cross-section of N-photon absorption.

The first term on the right-hand side (rhs) of Eq. (1) denotes the contribution to free electron generation due to avalanche ionization, a nonlinear process where a single charged particle initiates the ionization of others around it. The "seed" ions needed for the avalanche process to progress are formed by multi-photon ionization (MPI) quantified along with impact ionization in the second term of Eq. (1). MPI dominates the production of ions (and hence conduction band "free" electrons) in the first stages of a fs laser pulse [8]. After several fs, the avalanche process dominates, which leads to a drastic change in the optical properties of the material and is instrumental in the final surface modification.

Lenzner et al. [8] have experimentally determined the coefficients for fused silica: $a_i = 4 \pm 0.6$ cm^2/J, $\delta_N = 6 \times 10^{8 \pm 0.9}$ cm^{-3} ps^{-1}(cm^2/TW)^6 with $N = 6$, and barium aluminum borosilicate (BBS): $a_i = 1.2 \pm 0.4$ cm^2/J, $\delta_N = 7 \times 10^{17 \pm 0.5}$ cm^{-3} ps^{-1}(cm^2/TW)^3 with $N = 3$. A model has been proposed by Jiang and Tsai [9,10] based on Eq. (1) which has given ablation depths and crater shapes in good agreement with experiments. The model used for the present calculations draws heavily from that of [10] with exceptions to be noted during the discussion. The laser intensity within the material is described by

$$I(r,z,t) = \frac{2 \cdot F_{\text{peak}}}{\sqrt{\pi/\ln 2} \cdot t_p} [1 - R(r,t)]$$
$$\cdot \exp\left[-\frac{2 \cdot r^2}{r_0^2} - (4 \ln 2) \frac{t^2}{t_p^2} - \int_0^z \alpha(r,z,t) dz \right] \quad (2)$$

where t_p is the laser pulse duration, r_0 is the radius of the irradiated area, and α is the absorption coefficient of the material. Equation (2) provides for a Gaussian distribution of energy with space and time. The peak laser fluence, F_{peak}, is given by

$$F_{\text{peak}} = \frac{2 \cdot E_{\text{pulse}}}{\pi \cdot r_0^2} \quad (3)$$

where E_{pulse} is the total pulse energy.

The reflectivity of the material, R, is calculated as the maximum of the inherent, or "steady-state" reflectivity of the glass and the reflectivity of the plasma: $R(r,t) = \max(R_{ss}, R_p)$. Both values come from the complex refractive index of the material according to the Fresnel expression

$$R_p(r,t) = \frac{(n-1)^2 + k^2}{(n+1)^2 + k^2} \quad (4)$$

where n and k are the real and imaginary components of the refractive index, respectively. In the absence of plasma, the real refractive index for BBS of $n = 1.47$ gives $R_{ss} = 0.0362$. As the electron density evolves, the indices are calculated from the complex dielectric function of the material, $\varepsilon = \varepsilon_r + i\varepsilon_i$ by the relations

$$n = \sqrt{\frac{\varepsilon_r + \sqrt{\varepsilon_r^2 + \varepsilon_i^2}}{2}} \quad (5)$$

$$k = \sqrt{\frac{-\varepsilon_r + \sqrt{\varepsilon_r^2 + \varepsilon_i^2}}{2}} \quad (6)$$

The dielectric function of the plasma is calculated from Drude model [11]

$$\varepsilon_r = \left(1 - \frac{\omega_p^2(n_e)\tau^2}{1 + \omega^2\tau^2} \right) \quad (7)$$

$$\varepsilon_i = \left(\frac{\omega_p^2(n_e)\tau}{\omega(1 + \omega^2\tau^2)} \right) \quad (8)$$

where the laser frequency, $\omega = 2\pi c/\lambda$ with c as the speed of light in a vacuum and λ the laser wavelength. ω_p is the plasma frequency given by

$$\omega_p(n_e) = \sqrt{\frac{n_e(r,z,t)e^2}{m_e\varepsilon_0}} \quad (9)$$

and τ is the free electron relaxation time. The constant e is the electron charge, m_e is the electron mass, and ε_0 is the permittivity of free space.

The absorption coefficient in Eq. (2) has components due to free electron heating as well as ionization, given by

$$\alpha(r,z,t) = \alpha_H(r,z,t) + a_i n_e(r,z,t) U \quad (10)$$

Absorption due to free electron heating, α_H is

$$\alpha_H = \frac{4\pi k}{\lambda} \quad (11)$$

while U is the bandgap of the material. For fused silica, $U \approx 9$ eV. For BBS, $U \approx 4$ eV.

From [9], it is assumed that at the critical electron density, the plasma frequency is equal to the laser frequency. If a point in the material reaches the critical density, n_{cr}, a discrete amount of material is ablated

$$n_{\text{cr}} = \frac{4\pi^2 c^2 m_e \varepsilon_0}{\lambda^2 e^2} \quad (12)$$

From Eqs. (4)–(9), it is evident that the reflectivity of the material is dependent on two variables, the electron relaxation time, τ, and the electron density. Jiang and Tsai proposed a variable calculation of the relaxation time based on quantum treatment of the electron specific heat and electron temperature [16–18]. An investigation was conducted on the dependence of both relaxation time and electron density in R. It was found that the surface reflectivity varies greatly with electron density, a consequence of plasma generation, which has strong reflection and absorption properties. In contrast, reflectivity was essentially constant throughout a wide range of free electron relaxation time τ, varying significantly only when τ fell below 10 fs.

Metals with very large conduction band densities can exhibit relaxation times on the order of 1–10 fs [19], however, a dielectric with minimal conduction band density would expect to show much larger periods between electron/ion collisions. A relaxation time of the semiconductor silicon has been measured at >200 fs for moderate carrier densities [20]. Therefore, due to the order of magnitude increase in computational expense for a variable τ calculation, and the weak dependency on ablated volume, a constant relaxation time of 100 fs was used. The potential loss in accuracy due to the constant value of τ would not be removed even with a fully quantum calculation, which requires ionization state energies. These energies are unknown in a multi-element material with constantly changing internal energy, requiring an approximation regardless.

The numerical procedure involves calculating an electron density and intensity at each spatial point using the most recently updated reflectivity and absorption coefficient. Equations (4)–(11) are performed, and the density and intensity are updated. The cycle repeats until the densities and intensities have converged, completing the time step. Time step independence was achieved with values of $\Delta t = 0.01$ fs for a 100 fs pulse.

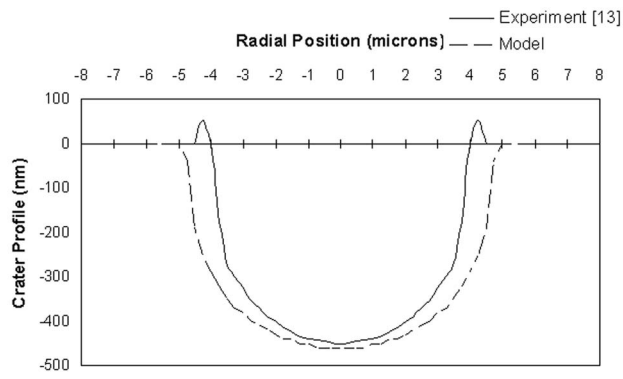**Fig. 1 Single shot ablated crater, $E_{pulse}=13.8$ μJ**

Theoretical Results

An experimental investigation of femtosecond ablation of borosilicate glass was conducted by Ben-Yakar and Byer [13] which offers excellent characterizations by which to verify the theoretical model. A quantitative evaluation of single shot ablated craters using three laser fluences with pulses of $\lambda=780$ nm and $t_p=200$ fs was carried out using an atomic force microscope. Figures 1 and 2 plot the experimental cross sections of the circular craters against the crater shapes predicted from the dielectric ablation model.

Figures 1 and 2 show a lip of material surrounding the experimental crater above the zero level of the substrate. This is assumed to be caused by a thermal after-effect of the excited electrons, which would heat the lattice and provoke both phonon and electron heat transfer after the pulse. If the lattice temperature is raised above the melting temperature of the material, a flow of molten glass would be subject to the local forces. The ablation model does not take into account fluid dynamics that may be the cause of the lip structure.

A notable result of the model is the successful prediction of a flat-bottom crater. Conventional thermal energy transport predicts shapes conforming to the Gaussian laser distribution, which result in round-bowl craters. Note the difference of scale in Figs. 1 and 2; depth in nanometers, radial position in micrometers.

The single shot ablation threshold of the borosilicate glass, or the minimum fluence at which material is removed, was found to be 2.6 J/cm^2 in air and 4.1 J/cm^2 in vacuum [13]. The dielectric ablation model, which does not consider the effect of a surrounding medium, predicts an ablation threshold of 3.6 J/cm^2.

The overall material removal during the pulse is highly dependent upon the optical response of the system. During the first few femtoseconds, multi-photon ablation dominates within the glass. The avalanche ablation effect increases nonlinearly as it becomes
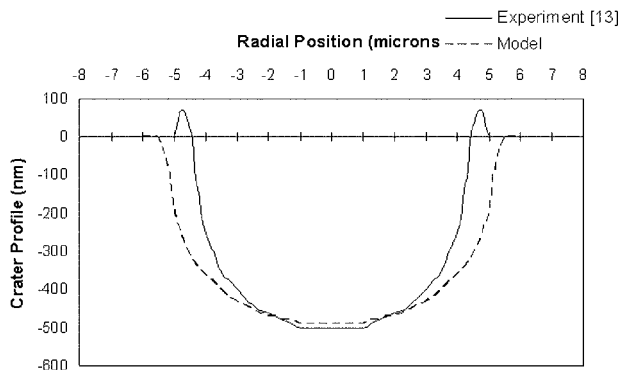

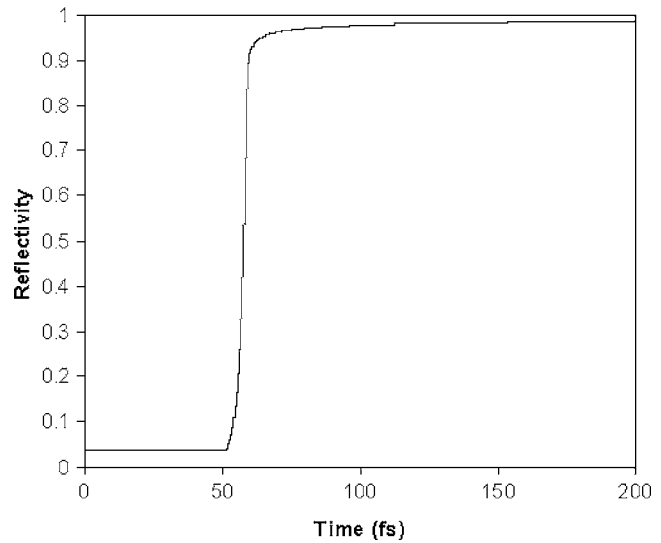**Fig. 2 Single shot ablated crater, $E_{pulse}=18.8$ μJ**

Fig. 3 Surface reflectivity at $r=0$ during 200 fs pulse

the dominant free-electron generation mechanism until the critical density is reached. At this point, plasma is formed at the surface as material is ejected. Figures 3 and 4 show how the surface reflectivity and absorption coefficient of the borosilicate glass transforms as the critical density is reached at approximately 50 fs. In the first stage of the pulse when the borosilicate is still transparent glass, the reflectivity retains its "standard" low value and the absorption coefficient is virtually zero. Near 50 fs, both values increase dramatically. The reflectivity levels to a nearly constant value where almost all energy is reflected, while the absorption of energy making it through the surface steadily increases as the plasma mass increases. Similar behavior was reported for fused silica [17].

Near-Field Enhanced Laser Ablation

The presence of a dielectric sphere on a sbstrate surface can enhance the electromagnetic field near the sphere boundary substantially [21,22]. An earlier paper reports on a method of quantifying the enhancement to provide an energy input for the ablation model using Mie's theory [22]. In this work, the finite-
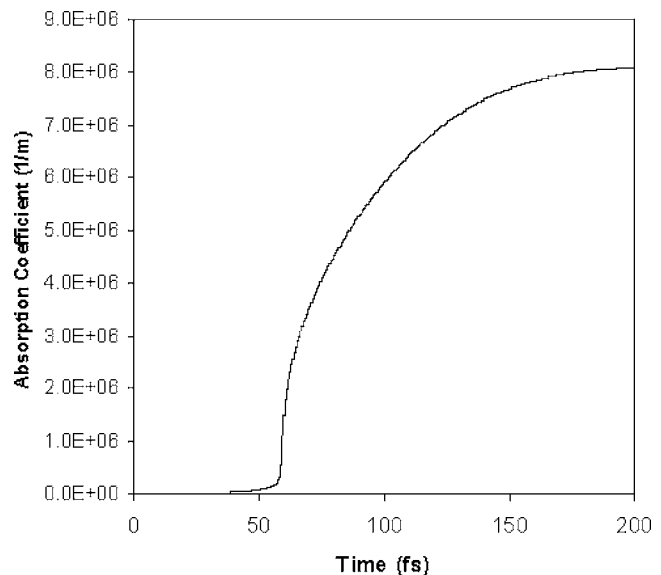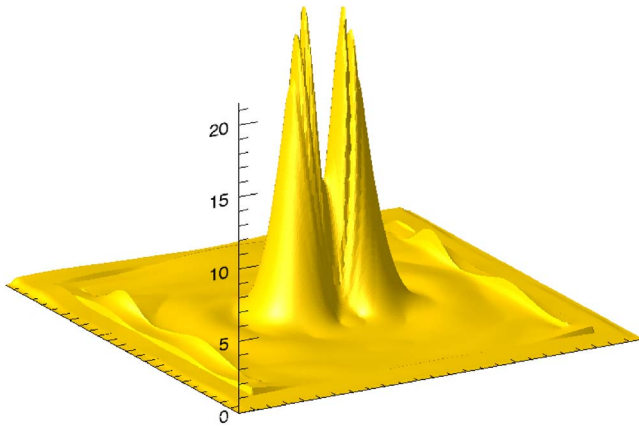

Fig. 4 Absorption coefficient at $r=0$, $z=0$ during 200 fs pulse

Fig. 5 Near-field enhanced laser intensity, λ=800 nm, r =880 nm

Fig. 6 Predicted ablation craters from near-field enhanced laser energy at three fluences
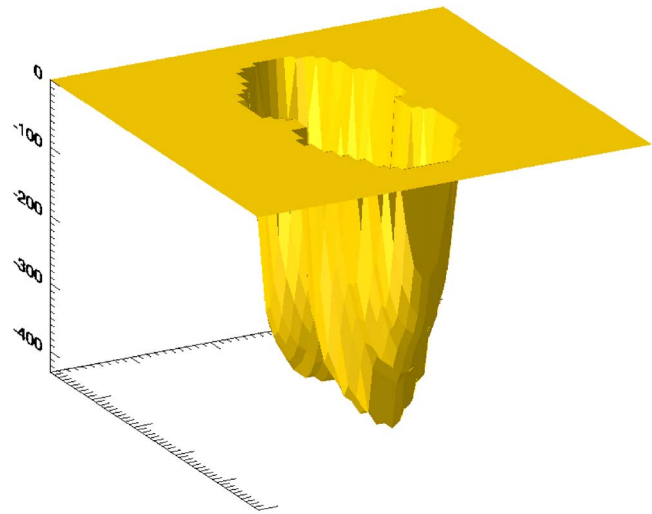
difference time-domain (FDTD) is employed in an in-house code to obtain the enhanced energy profile. The FDTD method is a widely popular technique of solving Maxwell's linear isotropic equations in complex environments where analytical solutions would be extremely difficult or impossible. While Mie's theory provides an exact solution for scattering of light from a sphere, the presence of the substrate and subsequent reflections add a level of complexity that is more easily tackled using FDTD. The Yee cell modeling geometry defines the mesh [23]. The incident radiation signal is generated using the total field/scattered field formulation [24], and the convolutional perfectly matched layer (CPML) absorbing boundary condition is employed at the boundary [25]. The details of the FDTD algorithm are covered in depth elsewhere [26,27] and, therefore, will not be addressed in this paper. The code was verified successfully against the analytical solution for a radiating dipole.

After initializing the property grids consistent with a vacuum, the sphere and substrate is placed in the environment by modifying the permittivity and permeability appropriately. The values used in this effort are $\mu=0.0005$ S/m and $\varepsilon=3.9^*\varepsilon_0$, where the permittivity of free space, $\varepsilon_0=8.8541878\times10^{-12}$ F/m.

Figure 5 presents a surface plot of the 3D FDTD simulation results predicting an enhanced energy profile "seen" by the glass substrate beneath a 1.76 μm diameter sphere irradiated by a λ =800 nm, $t_p=100$ fs laser pulse. The plotting range is a 2.5 μm × 2.5 μm square beneath the sphere.

Figure 5 indicates a peak level of enhancement of roughly twenty times the incident laser energy. The peak enhancement theoretically lowers the threshold for identifiable damage to 200–300 mJ/cm^2. The central dip in enhancement is due to the presence of the substrate, ostensibly because of reflection and interference effects. Without the Pyrex substrate, simulations predict a continuous, single "hump" with a slightly lower peak level of enhancement. Other researchers have presented results with similar central dips in near-field enhancement [15]. Figure 5 also predicts an asymmetrical angular energy distribution, a consequence of polarization. An ideal ablation simulation would be three-dimensional to account for the ovular enhanced energy profile, however the nondiffusive ablation mechanisms contained in the model dictate lateral independence of energy transport. Therefore, several 2D calculations can take the place of a single 3D calculation to determine the damage profile.

With the enhanced energy input, Eq. (2) becomes modified as follows:

$$I(r,z,t) = \frac{2 \cdot F_{peak}}{\sqrt{\pi/\ln 2} \cdot t_p} I_{FDTD}(r)[1 - R(r,t)]$$
$$\cdot \exp\left[-(4\ln 2)\frac{t^2}{t_p^2} - \int_0^z \alpha(r,z,t)dz \right] \quad (13)$$

where the additional $I_{FDTD}(r)$ term refers to the normalized level of enhancement relative to the incident plane wave prior to interaction with the sphere. The radial decay in the exponential argument is removed, as the spatial profile is accounted for in the FDTD results. Several pulses at a range of fluences were modeled with the enhanced laser input employed in Eq. (13). Figure 6 presents the damage profile predicted for a fluence of 950 mJ/cm^2. The oval-shaped crater has axes of length ~350 and ~700 nm, with a maximum depth of ~400 nm. The profile is in decent quantitative agreement with the experimental results to be presented, and qualitatively captures the ovular effect of polarization. A series of simulations conducted for the case of 330 mJ/cm^2 predicts crater dimensions of 160 × 380 nm × 200 nm depth. A predicted threshold fluence of 240 mJ/cm^2 was calculated, which matches neatly with both the theoretical adjustment discussed above as well as experimental results to be presented.

It is clear from Fig. 6 that the energy required to damage the glass substrate has been significantly reduced due to the presence of the sphere. A notable distinction between the damage profiles occurs with the enhanced energy, enabling depth to width ratios greater than unity to be achieved. The minimum obtainable dimensions predicted are also much smaller than those obtained with identical spheres using nanosecond laser pulses [15]. Laser enhancement due to the presence of the spheres breaks the optical diffraction limit, allowing optical machining at the submicrometer level. In this computational work, the diffraction limit has been undercut by an entire order of magnitude.

Experimental Study

Experiments have been conducted corresponding to the modelling parameters. Figure 7 shows the schematic of the experimental setup for the study. A borosilicate glass wafer sample is used as the substrate and monodisperse silica (SiO$_2$) spherical particles with a diameter of 1.76 μm were used. These silica particles are transparent to the near infrared light (800 nm wavelength of the laser used). The particle suspension was diluted with de-ionized water (DI) water and deposited on the glass substrate using a
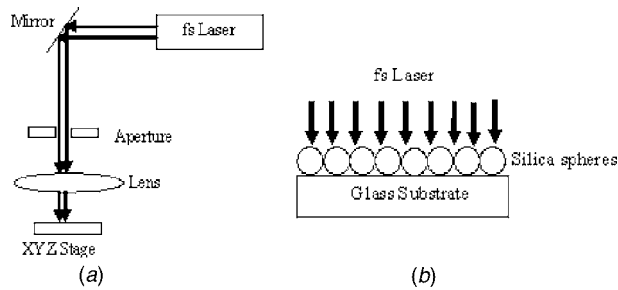
Fig. 7 Schematic of (a) experimental setup, (b) irradiation of the silica spheres on borosilicate glass substrate

dispenser. The sample was then stored at room temperature over a period of few hours for all the water solvent to evaporate. A titanium-doped sapphire (Ti:Sapphire), solid state laser with pulse at full width half maximum (FWHM) around 100 femtosecond (fs) and wavelength around 800 nm is used as the light source. The polarization of this fs laser pulse is linear and horizontal to the surface of the substrate. As shown in Fig. 7(b), a fs laser is irradiated at a zero angle of incidence onto the monolayer of silica
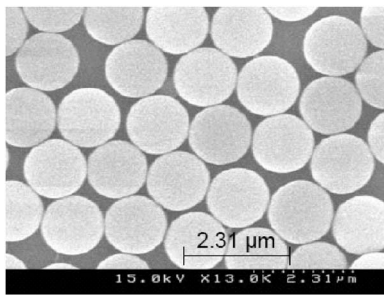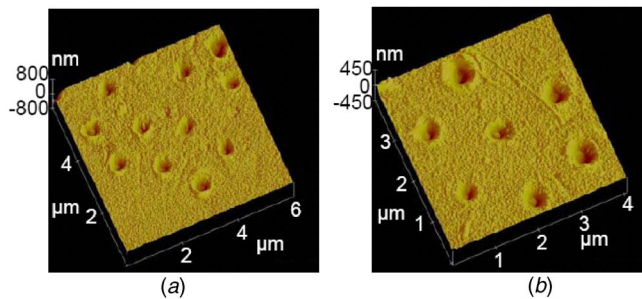

Fig. 8 SEM image of the monolayer of silica spheres with a diameter of 1.76 μm
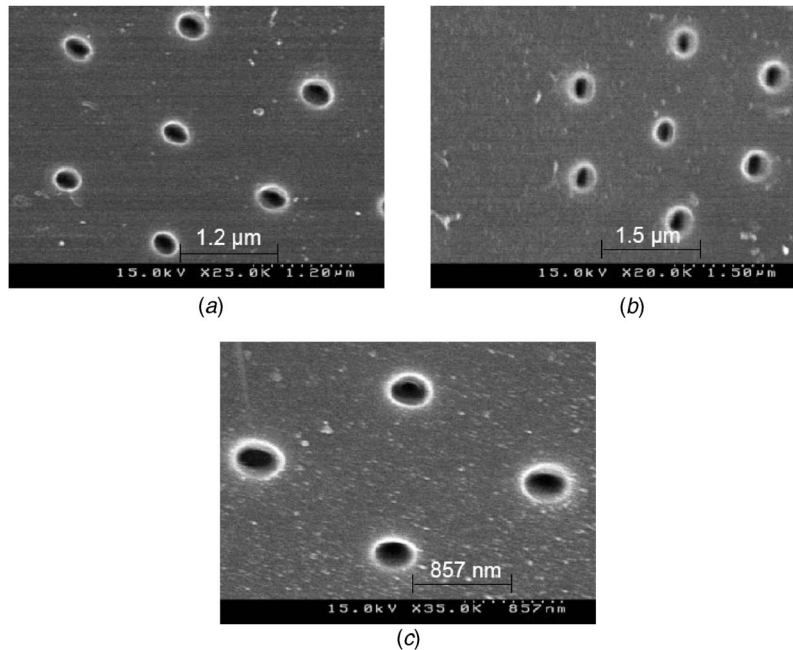
spheres deposited on the glass substrate. Different laser fluences were used to study the laser energy dependence of the nanostructures formed on the glass substrate. The laser energies used in the experiments varied from approximately 200 mJ/cm^2 to 1 J/cm^2. Zhou et al. [28] have recently used fs pulses to create subdiffraction limit modifications, though at much higher laser energies. The energy of the incident laser is varied by changing the delay time between the two pockel cells during the amplification using a synchronization and delay generator (SDG). Due to different delay times, the laser beam has to be compressed accordingly to maintain a constant pulse width and this is done by moving the compressor optics while monitoring the output laser beam pulse width with a single shot auto-correlator (SSA) and an oscilloscope. The glass substrate after laser nanostructuring was characterized by using a scanning electron microscope (SEM: Hitachi S4500) and the depths were measured by using an atomic force microscope (AFM: Nanoscope D3100). Figure 8 shows the SEM image of the monolayer of the silica spheres deposited on the borosilicate glass. To obtain good SEM images and in order to reduce the charging effects of the glass substrate a very thin layer of metal is deposited on the substrate.
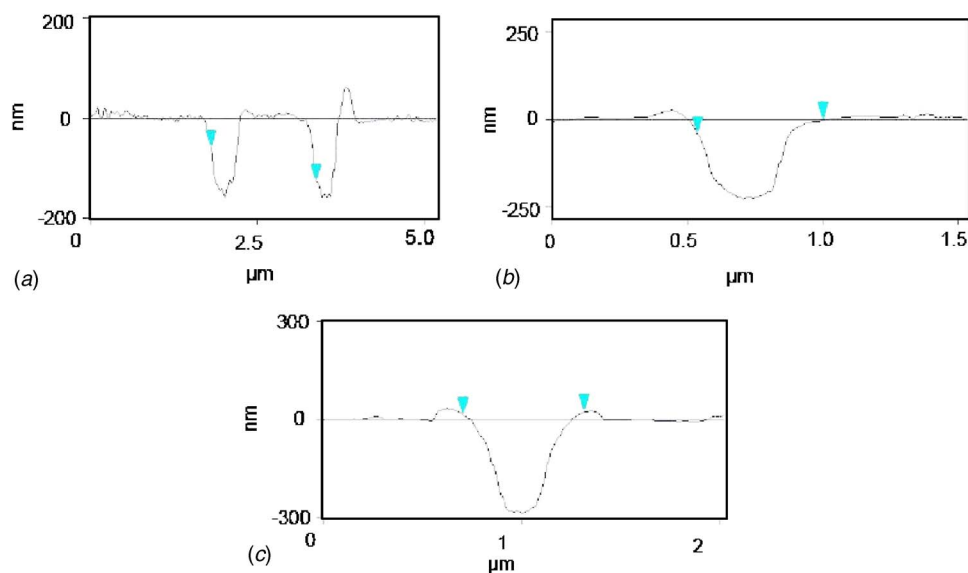
Figure 9 shows the SEM image of the nanostructures formed on the borosilicate glass by using the optical near-field enhancement for different laser fluences and one pulse irradiation. The nanostructures formed seem to be elliptical in shape as predicted in Fig. 6. This is due to the laser polarization, which plays an important role in optical enhancement and hole formation on glass substrate. Also it was found that most of the silica particles are removed from the substrate surface. These particles are removed from the surface mainly due to the deformation force and/or the high ablative force exceeding the particle-surface adhesion force [29]. Figure 9 shows that as the laser fluence decreases the nanostructures formed did not change in shape, unlike in some studies where sombrero-shape nanodents are formed at high laser fluences and bowl-shape nanodents are formed at low laser fluences [21,30]. Also, from Fig. 9 it can be seen that for the incident laser fluences of 330, 550, and 765 mJ/cm^2 the diameter of the holes along the major axis are approximately 250, 300, and 350 nm,

Fig. 9 SEM micrograph of the features formed on the glass substrate using microspheres with a single laser pulse irradiation (λ=800 nm and FWHM =100 fs) having laser fluence of (a) 330 mJ/cm^2, (b) 550 mJ/cm^2, and (c) 765 mJ/cm^2

Fig. 10 AFM profiles of the features formed on the glass substrate using microspheres with a single laser pulse irradiation ($\lambda=800$ nm and FWHM$=100$ fs) having laser fluence of (*a*) 230 mJ/cm^2 and (*b*) 405 mJ/cm^2

Conclusion

In summary, a model has been built using the Fokker-Planck equation to describe the ablation mechanism of dielectrics during femtosecond laser pulses. The ablation model is then employed to predict the response of borosilicate glass to an enhanced near-field electromagnetic intensity due to the presence of microspheres on the substrate surface. An experimental study has been performed to observe the nanostructures created on the surface for lower energy fluences. The features formed on the surface have diameters and depths in the order of 300 and 250 nm, depending on the incident laser intensity. The experimentally observed nanostructures is in good agreement with the theoretical predictions of surface modifications. Therefore, it is shown that the surface features can be created below the diffraction limit and at the nanoscale in a massively parallel fashion. Applications of this unique process include nanostructuring optical materials, bio-polymers, and biological materials.

respectively. Hence, the diameter of the nanostructures formed on the borosilicate glass increases with the laser fluence. Figure 10 shows the 3D AFM scanning profile of the nanostructure formed on the borosilicate glass and it can be seen that the structures formed have depths that are elliptical in shape which is in agreement with the SEM images (Fig. 9). Also the shapes of the nanostructures formed on the glass substrate remains the same for different laser fluences as seen earlier in Fig. 9.

Figure 11 shows the cross-sectional (or 2D) AFM profile of the nanostructures along their major axis and it can be seen clearly that for laser fluences of 230, 550, and 950 mJ/cm^2 the depth of the structures formed are approximately 180, 250, and 290 nm, respectively. These measured AFM cross-sectional profiles are in good agreement with the predicted profiles for similar incident laser energies, as shown in Fig. 6. From 2D AFM profiles we can observe that the bottom of the features along the major axis is flattened. The features can be explained by the above theoretical model predictions (Fig. 6) and also within the context of Mie's theory, which dictates strong forward scattering [31]. In general, the substrate modifications would be expected at the contact point due to the normal incidence of the laser pulse [32]. These nanostructures would then be driven by the intensity distribution in the surface plane.

Nomenclature

α = total absorption coefficient
α_H = abs. coeff. due to free electron heating
δ_N = cross-section of N-photon absorption
ε_r = real component of dielectric function
ε_i = imag. component of dielectric function
ε_0 = permittivity of free space
τ = free electron relaxation time
ω = laser frequency
a_i = avalanche ionization coefficient
c = speed of light

Fig. 11 AFM cross-section profiles of the features formed on the glass substrate using microspheres with a single laser pulse irradiation ($\lambda=800$ nm and FWHM$=100$ fs) having laser fluence of (*a*) 230 mJ/cm^2, (*b*) 550 mJ/cm^2, and (*c*) 950 mJ/cm^2

e = electron charge
F_{peak} = peak laser fluence
m_e = electron mass
n_e = free electron density
R = reflectivity
R_p = plasma reflectivity
R_{ss} = inherent reflectivity
t_p = laser pulse duration
U = bandgap

References

[1] Zhang, J., Sugioka, K., and Midorikawa, K., 1999, "High-Quality and High-Efficiency Machining of Glass Materials by Laser-Induced Plasma-Assisted Ablation Using Conventional Nanosecond UV, Visible, and Infrared Lasers," Appl. Phys. A, **69**, pp. 879–882.

[2] Park, D. S., Cho, M. W., Lee, H., and Cho, W. S., 2004, "Micro-Grooving of Glass Using Micro-Abrasive Jet Machining," J. Mater. Process. Technol., **146**, pp. 234–240.

[3] Yan, B. H., Wang, A. C., Huang, C. Y., and Hunag, F. Y., 2002, "Study of Precision Micro-Holes in Borosilicate Glass Using Micro EDM Combined with Micro Ultrasonic Vibration Machining," Int. J. Mach. Tools Manuf., **42**, pp. 1105–1112.

[4] Zhang, J., Sugioka, K., and Midorikawa, K., 1998, "High-Speed Machining of Glass Materials by Laser Induced Plasma Assisted Ablation Using a 532 nm Laser," Appl. Phys. A: Mater. Sci. Process., **67**, pp. 499–501.

[5] Nikumb, S., Chen, Q., Li, C., Reshef, H., Aheng, H. F., Qiu, H., and Low, D., 2005, "Precision Glass Machining, Drilling and Profile Cutting by Short Pulse Lasers," Thin Solid Films, **477**(1–2), pp. 216–221.

[6] Youn, S. W., and Kang, C. G., 2005, "Maskless Patterning of Borosilicate Glass Nanoindentation-Induced Etch-Hillock Surface Using Phenomena," J. Non-Cryst. Solids, **351**(37–39), pp. 3065–3074.

[7] Hirano, M., Kawamura, K. I., and Hosono, H., 2002, "Encoding of Holographic Grating and Periodic Nano Structure by Femtosecond Laser Pulse," Appl. Surf. Sci., **197**, pp. 688–698.

[8] Lenzner, M., Kruger, J., Sartania, S., Cheng, Z., Spielmann, Ch., Mourou, G., Kautek, W., and Krausz, F., 1998, "Femtosecond Optical Breakdown in Dielectrics," Phys. Rev. Lett., **80**, pp. 4076–4079.

[9] Stuart, B. C., Feit, M. D., Herman, S., Rubenchik, A. M., Shore, B. W., and Perry, M. D., 1995, "Laser-Induced Damage in Dielectrics With Nanosecond to Subpicosecond Pulses," Phys. Rev. Lett., **74**, pp. 2248–2251.

[10] Perry, M. D., Stuart, B. C., Banks, P. S., Feit, M. D., Yanovsky, V., and Rubenchik, A. M., 1999, "Ultrashort-Pulse Laser Machining of Dielectric Materials," J. Appl. Phys., **85**, pp. 6803–6810.

[11] Campbell, S., Dear, F. C., Hand, D. P., and Reid, D. T., 2005, "Single-Pulse Femtosecond Laser Machining of Glass," J. Opt. A, Pure Appl. Opt., **7**, pp. 162–168.

[12] Ben-Yakar, A., Byer, R. L., Harkin, A., Ashmore, J., Stone, H., Shen, M., and Mazur, E., 2003, "Morphology of Femtosecond-Laser-Ablated Borosilicate Glass Surfaces," Appl. Phys. Lett., **83**(15), pp. 3030–3032.

[13] Ben-Yakar, A., and Byer, R. L., 2004, "Femtosecond Laser Ablation Properties of Borosilicate Glass," J. Appl. Phys., **96**, pp. 5316–5323.

[14] Qiu, T. Q., and Tien, C. L., 1993, "Heat Transfer Mechanisms During Short-Pulse Laser Heating of Metals," ASME J. Heat Transfer, **115**, pp. 835–841.

[15] Chimmalgi, A., Grigoropoulos, C. P., and Komvopolous, K., 2005, "Surface Nanostructuring by Nano-/Femtosecond Laser-Assisted Scanning Force Microscopy," J. Appl. Phys., **97**, p. 104319.

[16] Jiang, L., and Tsai, H. L., 2004, "Prediction of Crater Shape in Femtosecond Laser Ablation of Dielectrics," J. Phys. D, **37**, pp. 1492–1496.

[17] Jiang, L., and Tsai, H. L., 2005, "Energy Transport and Material Removal in Wide Bandgap Materials by a Femtosecond Laser Pulse," Int. J. Heat Mass Transfer, **48**, pp. 487–499.

[18] Kruer, W. L., 1987, *The Physics of Laser Plasma Interaction*, Addison Wesley, New York.

[19] Kittel, C., 1996, *Introduction to Solid State Physics*, Wiley, New York.

[20] Sjodin, T., Petek, H., and Dai, H.-L., 1998, "Ultrafast Carrier Dynamics in Silicon: A Two-Color Transient Reflection Grating Study on a (111) Surface," Phys. Rev. Lett., **81**, pp. 5664–5667.

[21] Lu, Y., Theppakuttai, S., and Chen, S. C., 2003, "Marangoni Effect in Nanosphere-Enhanced Laser Nanopatterning of Silicon," Appl. Phys. Lett., **82**, pp. 4143–4145.

[22] Heltzel, A., Theppakuttai, S., Chen, S. C., and Howell, J. R., 2005, "Analytical and Experimental Investigation of Laser Nanoscale Surface Modification," ASME J. Heat Transfer, **127**(11), pp. 1231–1235.

[23] Yee, K. S., 1966, "Numerical Solution of Inital Boundary Value Problems Involving Maxwell's Equations in Isotropic Media," IEEE Trans. Antennas Propag., **14**, pp. 302–307.

[24] Umashankar, K. R., and Taflove, A., 1982, "A Novel Method to Analyse Electromagnetic Scattering of Complex Objects," IEEE Trans. Electromagn. Compat., **24**, pp. 397–405.

[25] Roden, J. A., and Gedney, S. D., 2000, "Convolutional PML (CPML): An Efficient FDTD Implementation of the CFS-PML for Arbitrary Media," Microwave Opt. Technol. Lett., **27**, pp. 334–339.

[26] Taflove, A., and Hagness, S., 2005, *Computational Electrodynamics, The Finite-Difference Time-Domain Method*, 3rd ed., Artech House, Boston.

[27] Sullivan, D., 2000, *Electromagnetic Simulation Using the FDTD Method*, Wiley, New York.

[28] Zhou, Y., Hong, M. H., Fuh, JYH, Lu, L., Luk'yanchuk, B. S., Wang, Z. B., Shi, L. P., and Chong, T. C., 2006, "Direct Femtosecond Laser Nanopatterning of Glass Substrate by Particle-Assisted Near-Field Enhancement," Appl. Phys. Lett., **88**, p. 023110.

[29] Zheng, Y. W., Luk'yanchuk, B. S., Lu, Y. F., Song, W. D., and Mai, Z. H., 2001, "Dry Laser Cleaning of Particles from Solid Substrates: Experiments and Theory," J. Appl. Phys., **90**, pp. 2135–2142.

[30] Wang, Z. B., Hong, M. H., Luk'yanchuk, B. S., Huang, S. M., Wang, Q. F., Shi, L. P., and Chong, T. C., 2004, "Parallel Nanostructuring of GeSbTe Film With Particle Mask," Appl. Phys. A: Mater. Sci. Process., **79**, pp. 1603–1606.

[31] Ikawa, T., Mitsuoka, T., Hasegawa, M., Tsuchimori, M., Watanabe, O., and Kawana, Y., 2001, "Azobenzene Polymer Surface Deformation Due to the Gradient Force of the Optical Near Field of Monodispersed Polystyrene Spheres," Phys. Rev. B, **64**, p. 195408.

[32] Wang, Z. B., Hong, M. H., Luk'yanchuk, B. S., Lin, Y., Wang, Q. F., and Chong, T. C., 2004, "Angle Effect in Laser Nanopatterning With Particle-Mask," J. Appl. Phys., **96**(11), pp. 6845–6850.